Bull. Mater. Sci. (2019) 42:58
https://doi.org/10.1007/s12034-019-1766-8

Structural, morphological and dielectric traits of $Zr_{1-x}Ca_xTiO_4$ ($x = 0$, 0.05, 0.10, 0.15 and 0.2) ceramics

NAADIA AKHTAR[1,*], HAFIZ MUHAMMAD RAFIQUE[1], SHAHID ATIQ[2], SANA ASLAM[1], AAMIR RAZAQ[3] and MURTAZA SALEEM[4]

[1]Department of Physics, School of Physical Sciences (SPS), University of the Punjab, Quaid-e-Azam Campus, Lahore 54590, Pakistan
[2]Center of Excellence in Solid State Physics, University of the Punjab, Quaid-e-Azam Campus, Lahore 54590, Pakistan
[3]Department of Physics, COMSATS Institute of Information Technology, Lahore 54000, Pakistan
[4]Department of Physics, School of Science and Engineering (SSE), Lahore University of Management Sciences (LUMS), Lahore 54792, Pakistan
*Author for correspondence (naadiaakhtar@gmail.com)

MS received 25 April 2018; accepted 12 September 2018; published online 6 March 2019

Abstract. The influence of Ca doping on structural, morphological and dielectric characteristics of $Zr_{1-x}Ca_xTiO_4$ ($x = 0$, 0.05, 0.10, 0.15 and 0.2) ceramics has been planned in this effort. Un-doped and Ca-doped $ZrTiO_4$ (ZT) have been synthesized through a sol–gel auto-combustion approach. The orthorhombic phase of ZT and Ca-doped ZT is confirmed through X-ray diffraction patterns. The variation in structural morphology and particle size due to Ca incorporation in ZT has further been revealed by field emission scanning electron microscopy. The investigation showed that the size of the particle gradually reduced from 0.5 to 0.125 μm with the increase of Ca content. It was confirmed from Fourier transform infrared spectroscopy that organic content was not found in the prepared samples. Dielectric constant, dielectric loss factor and tangent loss reduce with the increase in frequency and increase in Ca content. These dielectric parameters show independency at a higher frequency. The modulus plots confirmed that the capacitive parts were relatively independent of the frequency, whereas ac conductivity exhibited frequency dependent behaviour i.e., an increase with Ca concentration and with increasing frequency. The impedance plots revealed the resistance dominance due to the grain boundary effect.

Keywords. XRD; dielectric properties; EDS; FE-SEM; FTIR; sol–gel synthesis.

1. Introduction

Energy crunch is a main problem worldwide. There is a need to reduce the size of devices which are portable, store more data and consume less energy. These types of devices include dielectric resonators, frequency filters, capacitors and small size sensors [1,2]. A material with suitable composition which offers excellent dielectric properties is required to attain the above mentioned goal. Usually, mixed metal oxides (comprising associating ABO_4 compound, where two dissimilar metal cations i.e., A and B connected with the oxygen) provide a striking approach as dielectric materials to create innovative crystallographic phases with more superior properties than the original ones [3]. Amongst the different metal oxides, a mixture of titanium and zirconium has received considerable attention in recent years. ZrO_2–TiO_2 composite oxides exhibit high temperature stability, good mechanical strength and high dielectric constant [4]. Zirconium and titanium have different ionic radii i.e., 0.72 Å for Zr^{4+} and 0.605 Å for Ti^{4+}, although their cations are isovalent. They can form metal oxides of several kinds, for instance $ZrTiO_4$ (ZT), a stoichiometric compound made under atmospheric pressure [5]. In general, ZT is a ceramic natured material which exhibits excellent properties for applications for example, small size sensors [6], ceramic capacitors and resonators for telecommunication [7,8] purposes because of its slight loss, excellent high temperature stability and greater Q value. In addition, the doping of a material of any kind at any site (A or B) affects the dielectric properties. However, alkaline earth metals may be used as dopant aimed at IV–IV, III–V, II–VI and I–VII binary composites to control charge to comprehend devices for energy storage for capacitor applications.

Previous work on ZT with Sn addition has been documented as an excellent candidate for the applications of dynamic random access memory due to its high dielectric constant and low leakage current [9,10]. Recently, materials such as $Ba_2Ti_9O_{20}$ [11], $BaTi_4O_9$ [12], $Zr_{0.75}Hf_{0.25}TiO_4$ and $Zr_{0.8}Sn_{0.2}TiO_4$ [13] have been examined which offer higher dielectric constant at 4 GHz with slight loss. However, the constituents (Sr, Ca)[(Li, Nb), Ti]O_3 and (Ca, Sr)(Ba, Zr)O_3 offered low quality factor at high frequency [14]. The performance limitations resulting from this lower dielectric constant remain to be determined. Different techniques have been employed to synthesize ZT samples to obtain

different properties, such as co-precipitation, hydrothermal, mechanical mixing methods, DC magnetron sputtering method [15–17], phonon confinement model [19] and molten salt synthesis route [18]. But these techniques are costly and time consuming. Therefore, the sol–gel auto-combustion technique is employed to synthesize pure ZT ceramics, which usually crystallizes at a lower temperature as compared to the above stated methods. This method gives pure ceramics and their microstructure is relatively easily modified.

In this paper, we present the synthesis of $Zr_{1-x}Ca_xTiO_4$ ($x = 0$, 0.05, 0.10, 0.15 and 0.2) ceramics using the sol–gel auto-combustion process. Results and analysis of the structural, morphological and dielectric properties i.e., dielectric constant (ε'), dielectric loss (ε''), tangent loss (tan δ), ac conductivity, electric modulus, imaginary and real impedance of ZT and Ca-doped ZT measured in 20 Hz to 20 MHz range of frequency are studied in depth.

2. Experimental

Zirconium nitrate ($Zr(NO_3)_4{\cdot}5H_2O$, 99%, UNI-CHEM), titanium (IV) butoxide ($Ti(OBut)_4$, 97%, Aldrich) and calcium nitrate ($Ca(NO_3)_2{\cdot}4H_2O$, 99.5%, BDH Chemicals) are used as starting raw materials. Eighty millilitre solution of these ingredients, leading to the composition of the form, $Zr_{1-x}Ca_xTiO_4$ ($x = 0$, 0.05, 0.10, 0.15 and 0.2) is prepared by the process described elsewhere [20]. The process led to the formation of a dark brown coloured powder. This powder was ground to obtain a fine form for 30 min. The powder was calcined for 2 h at 800°C and then for 1 h at 1200°C to remove any organic content from it. The colour of the prepared series was dark brown which changed to pure white after calcination. Again, this calcined powder was ground to retain homogeneity. Pellets having variable values of thickness (1.39, 2.16, 1.48, 1.20 and 0.82 mm) and 10 mm of diameter were prepared by applying a 4.5 tonne force using an Apex hydraulic press.

To estimate the structural aspects of the prepared powder, X-ray diffraction (XRD) (Rigaku 11-A XRD/Max Diffractometer) was used with Cu K_α radiation of $\lambda = 1.540598$ Å for angle 2θ range of 10–75°. To determine the organic content present in the samples, Fourier transform infrared (FTIR) spectroscopy (Agilent Technologies Cary 630 FTIR) is used. To evaluate the elemental composition and the morphological aspects of the prepared samples, energy dispersive X-ray method (JEOL 35CF EDS and XS-3400N Hitachi SEM) and field emission scanning electron microscope (FE-SEM), respectively are used. To calculate the dielectric properties of the prepared pellets, an impedance analyser (precision impedance analyser Wayne Kerr 6500B) is used at room temperature (RT) in the 20 Hz to 20 MHz frequency range.

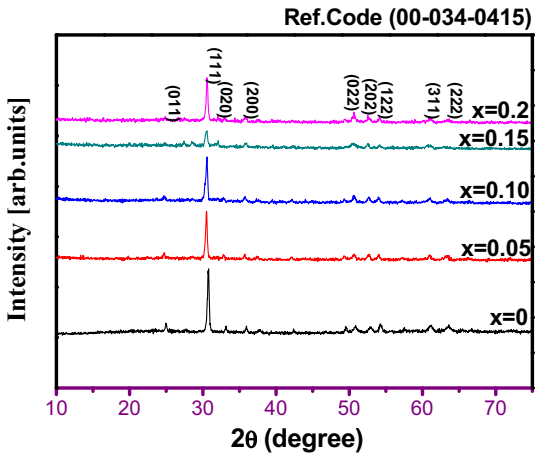

Figure 1. XRD patterns of ZT and Ca-doped ZT.

3. Results and discussion

Figure 1 displays the XRD patterns of $Zr_{1-x}Ca_xTiO_4$ ($x = 0$, 0.05, 0.10, 0.15 and 0.2) ceramics calcined at 1200°C. All the detectable peaks are indexed according to JCPDS card 00-034-0415 [21] showing a pure orthorhombic phase with a *Pnab* 60 space group of ZT and in this pattern impurity peaks associated with the secondary phase are not detected. Moreover, with $x = 0.05$, 0.10, 0.15 and 0.2 contents of Ca, all the peaks are well accorded with the above stated card maintaining the orthorhombic phase.

Generally, lattice distortion occurs as a result of defects (i.e., interstitial, vacancies, structural transformation, substitutions etc.) which become a source to shift in the XRD peak positions. Depending on the kind of strain present in the crystal i.e., tensile or compressive strain, the position of the peak shifts to a higher or lower angle, respectively [22]. As the ionic radius of Ca is greater than that of Zr, Ca substituting Zr in lattice of ZT may result in a tensile strain along with expansion of the crystallite size. Meanwhile, there is a slight regular shift in the patterns towards lower angles with increasing x due to a comparatively greater ionic radius of Ca^{2+} compared to Zr^{2+} as shown in table 1. With increasing Ca content, the intensity of the peaks improves which determines the enhanced crystallinity of the planned sample. Table 2 shows the variations in lattice parameters, cell volume and crystallite size with respect to x. The lattice parameter and the cell volume are observed to increase with the increase in x due to the substitution of Ca^{2+} (1.14 Å, coordination number = 6) for Zr^{2+} (0.72 Å, coordination number = 6) [23]. The crystallite size is calculated for the most intense peak (111) by using the following relation:

$$D = k\lambda/\beta\cos\theta, \tag{1}$$

where k (dimensionless quantity) is a shape factor which is equal to 0.95, λ represents the wavelength of Cu K_α radiation and β symbolizes the full width at half maximum, which

Table 1. Shift in the diffraction angle (2θ-degrees) for three representative planes of undoped and Ca-doped ZT series.

Crystal planes	$ZrTiO_4$	$Zr_{0.95}Ca_{0.05}TiO_4$	$Zr_{0.9}Ca_{0.10}TiO_4$	$Zr_{0.85}Ca_{0.15}TiO_4$	$Zr_{0.8}Ca_{0.20}TiO_4$
011	24.966	24.912	24.842	24.819	24.712
111	30.786	30.721	30.652	30.585	30.575
020	32.688	32.676	32.606	32.537	32.446

Table 2. Lattice parameter (Å), cell volume (Å^3) and crystallite size of undoped and Ca-doped ZT series.

x	Crystal symmetry	a (Å)	b (Å)	c (Å)	Cell volume (Å^3)	Crystallite size (nm)
0	Orthorhombic	5.0007	5.4762	4.6958	128.5937	30.12
0.05	Orthorhombic	5.0106	5.4779	4.7118	129.3274	31.08
0.10	Orthorhombic	5.0158	5.4893	4.7275	130.1633	30.13
0.15	Orthorhombic	5.0391	5.5008	4.7276	131.0447	21.51
0.20	Orthorhombic	5.0020	5.5158	4.7532	131.1409	32.08

An error of ±0.0005 is expected in the calculations of lattice parameters.

defines the dependence on the crystallite size. Table 2 shows the increase in the crystallite size from 30.12 to 31.08 nm with substitution of $x = 0.05$ molar concentration of Ca in the prepared samples. This trend once more is due to the variance of ionic radii of both the host and the dopants. Though variation in the crystallite size is observed for the 0.10–0.2 samples, the standard deviation of the crystallite size is found to be 3.81 nm.

FTIR examination of the $Zr_{1-x}Ca_xTiO_4$ ceramics with $x = 0$, 0.05, 0.10, 0.15 and 0.2 concentration has been conducted in the range of 650–4000 cm^{-1} at 1200°C as shown in figure 2. Figure 2a shows that there is no peak at range of 4000–1550 cm^{-1} for the samples prepared before calcination. It reflects that there is a complete exclusion of functional groups (i.e., OH and NH) in the above stated range. Though at 1541 cm^{-1} and 1390 cm^{-1} range, two peaks are detected for $x = 0-0.2$ samples which correspond to C=O and C–N bonds, as predicted in figure 2a, which have already been observed somewhere else [24]. However, the intensity of both the bonds rapidly decreases for the results achieved after calcination at 1200°C indicating a thorough combustion or vapourization of organic contents, as shown in figure 2b. This corroborates the XRD results presenting complete combustion (i.e., organic bonds do not exist in the prepared samples) in the above mentioned range.

A typical microstructure of $Zr_{1-x}Ca_xTiO_4$ ($x = 0.05$, 0.10, 0.15 and 0.2) is shown in figure 3. It exhibits the morphology of the samples i.e., ZT and Ca-doped ZT and their equivalent energy-dispersive spectroscopy (EDS) examination. Large and small sized particles at 50,000 magnification are seen in figure 3a. The average particle size varies

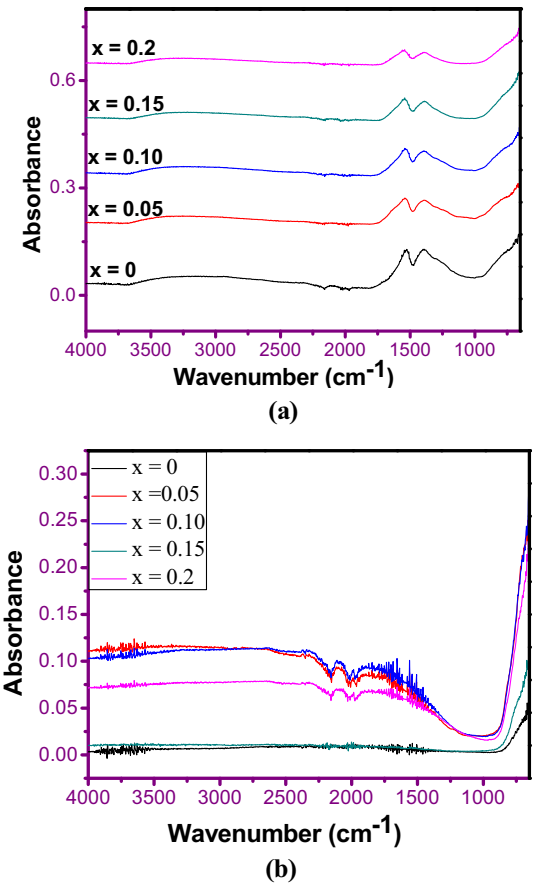

Figure 2. FTIR analysis of ZT and Ca-doped ZT (**a**) before calcination and (**b**) after calcination.

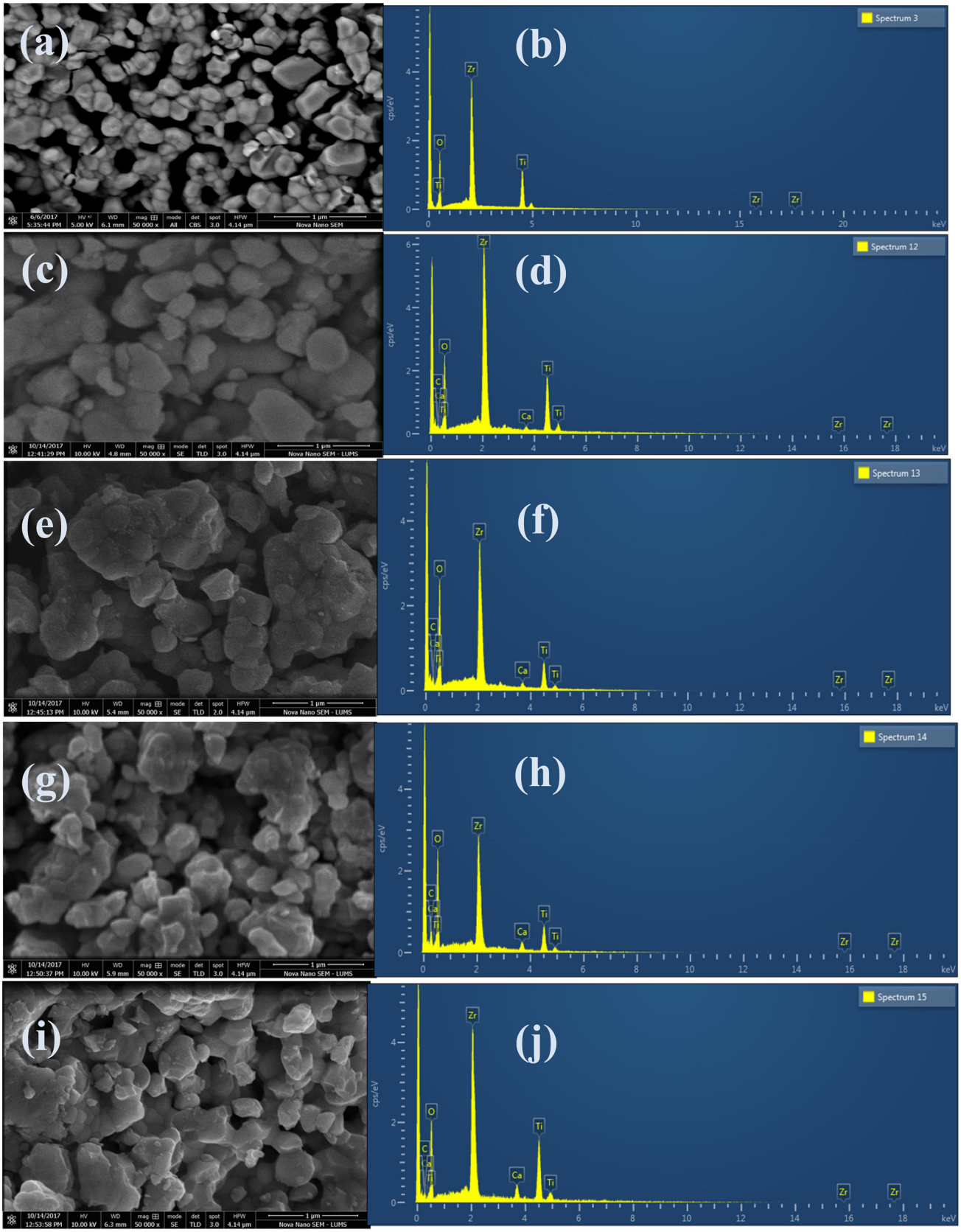

Figure 3. FE-SEM images of (**a**) ZT, (**c**, **e**, **g** and **i**) Ca-doped ZT pellet at 50,000 magnification and (**b**, **d**, **f**, **h** and **j**) their EDS analysis.

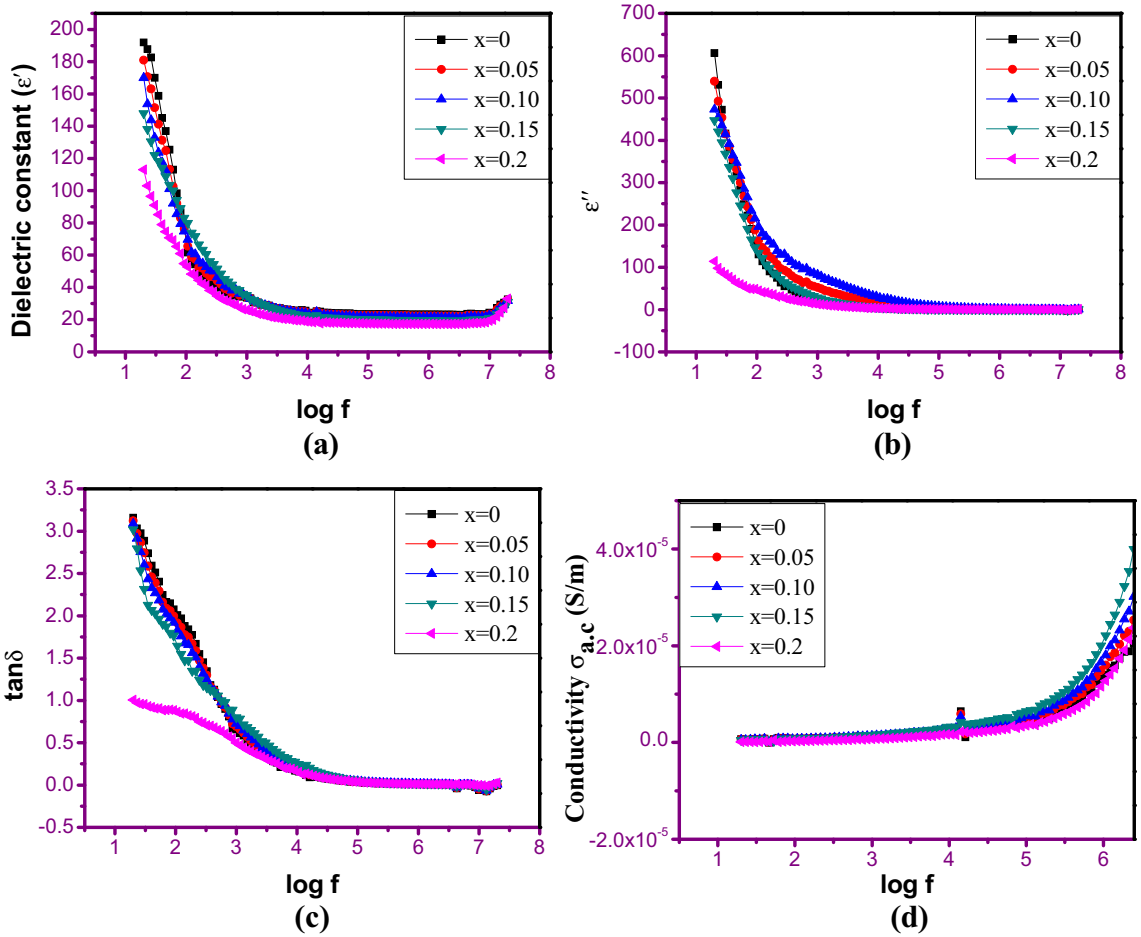

Figure 4. Frequency dependence of (**a**) dielectric constant (ε'), (**b**) dielectric loss (ε''), (**c**) tangent loss (tan δ) and (**d**) ac conductivity for $Zr_{1-x}Ca_xTiO_4$ ($x = 0$, 0.05, 0.10, 0.15 and 0.2) samples at RT.

from 0.5 to 0.125 μm as shown in figure 3b–e which is irregular in morphology. With increasing Ca molar concentration, homogeneity of the particles improves which is indicative of the fact that the crystallinity of the particles increases, as confirmed from the XRD analysis, as well. EDS analysis is employed to determine the chemical elements existing in the prepared series. Figure 3b, d, f, h and j shows EDS spectra for ZT and Ca-doped ZT which ratify the existence of Ti, O, Zr and Ca in the samples according to their stoichiometric constituents associated with their empirical formula. One additional peak of carbon is also found in these spectra which was not observed in the XRD patterns.

Figure 4a displays the dielectric constant for $Zr_{1-x}Ca_xTiO_4$ ($x = 0.05$, 0.10, 0.15 and 0.2) measured at RT in the 20 Hz to 20 MHz frequency range. The dielectric constant is high in a lower frequency region then decreases on increasing frequency and increasing Ca contents specifically at $x = 0-0.2$. The observed dielectric behaviour i.e., the dielectric constant decrease with frequency is ascribed to the Maxwell–Wagner interfacial polarization which is confirmed by the Koop's phenomenological model [25,26]. The typical dielectric behaviour consists of low conducting grain boundaries which are separated from the highly conducting grains [27]. This happens in dipolar relaxation i.e., the charge carriers transferring through the dielectric become trapped alongside the defect site and create the opposite charges in its locality. Consequently, they slow down and in this way there is a reasonable decrease in dielectric constant with frequency. Figure 4b shows that the loss factor sharply decreases with frequency. High dielectric loss is observed at a lower frequency which might be because of mobile charges present inside the ceramic matrix. There is no ion dispersion in the applied electric field direction because of fast periodic field reversal at high frequency [28]. Therefore, due to accumulation of the charges, polarization decreases, as a result, the value of the dielectric loss factor decreases. Generally, during dielectric study, it is believed that the dielectric constant at high frequency is mostly related to dipolar relaxation. However, the contribution of the interfacial or space charge polarization becomes extra important in both the dielectric loss factor and the dielectric constant at low frequency. The difference in the relaxation time, with the change in Ca dopant concentration, might be due to electric charges being displaced inside the matrix [29].

Moreover, figure 4c exhibits the $\tan\delta$ noted at RT for $Zr_{1-x}Ca_xTiO_4$ with $x = 0-0.2$ as a function of frequency. The decrease in tangent loss is detected with the increase in Ca content and frequency. Tangent loss at lower frequency is high. This can be attributed to the dominancy of grain boundary which is highly resistive, is accredited with impurities, crystal defects and moisture. But, grain having low resistance is dominant in a high frequency region because less energy is required to transfer electrons between two different A-site ions, and hence dielectric loss is low [30].

Generally, the high and low frequency regions are parted by a variation in slope at a specific frequency. This particular frequency is called the hopping frequency. The plot of ac conductivity *vs.* frequency for Ca-doped ZT series is shown in figure 4d. This figure shows the increase in the ac conductivity with increasing frequency and increasing Ca concentration in the ZT sample. Here a transport mechanism occurs i.e., as the applied electric field frequency increases, ac conductivity also increases. This might be a result of increase in the hopping between the charge carriers [31]. The ac conductivity decreases with increasing crystallite size using 0–0.2 molar concentration of Ca in the parent material. These reductions in the ac conductivity arise with the decrease in the hopping distance [32].

Figure 5a and b respectively exhibits a difference in the real (Z') and the imaginary (Z'') parts of impedance for $Zr_{1-x}Ca_xTiO_4$ ($x = 0-0.2$) ceramics with frequency. From the plots, it is seen that Z' monotonically decreases with increasing frequency and reaches a point where it becomes independent of frequency. The value of Z' at low frequency is high which indicates larger polarization present in the material. The graph also shows that the grain boundaries resistance turn into conducting and grain boundaries are not relaxed for the measurement taken at the highest range of frequency. The Z'' plot signifies that the impedance decreases with increasing frequency and with increasing molar concentration of Ca and it also becomes independent at higher frequency as presented in figure 5b. This might be due to the reason that at high frequency under the applied external electric field, the space charge accumulation is released at the grain boundaries of uniform phases present in the material. This decrease in the impedance value similarly shows the increase in the ac conductivity with frequency and addition of Ca content. Usually complex impedance analysis is used to characterize material's electrical property and their interfaces by using electronic conducting electrodes. Hence, it may also be used to explore the dynamics of the mobile or bound charges in the interfacial or bulk regions of any type of liquid or solid material: dielectrics, ionic, mixed ionic-electronic and even semiconducting material. Mostly real ceramics consist of two regions i.e., grain boundary and grain regions. These regions have individually different physical properties. Modulus and impedance spectra are used to observe the above mentioned types of regions. In ceramic materials, the conduction process of grain boundary is emphasized

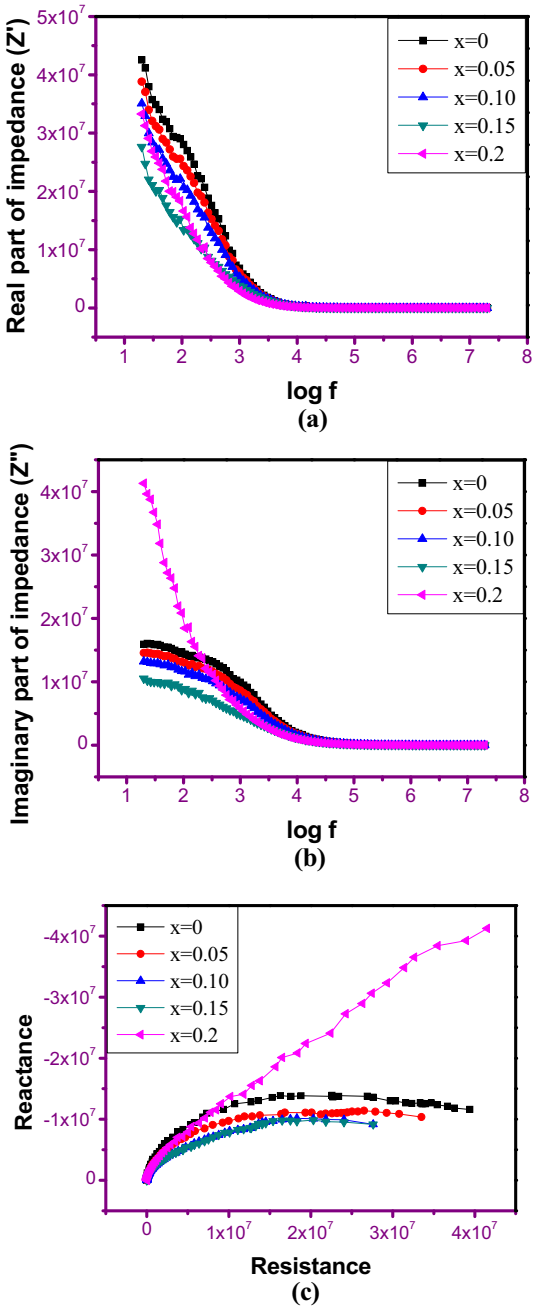

Figure 5. Frequency dependence of (**a**) real part of impedance, (**b**) imaginary part of impedance and (**c**) Nyquist plot of $Zr_{1-x}Ca_xTiO_4$ ($x = 0$, 0.05, 0.10, 0.15 and 0.2) samples.

by impedance formalism, while electric modulus formalism dominates the bulk effects [33]. Therefore, in the present study, these two formalisms are used to determine the electrical property of the material. A Cole–Cole plot (Nyquist plot) for the $Zr_{1-x}Ca_xTiO_4$ ($x = 0$, 0.05. 0.10, 0.15 and 0.2) sample at RT is displayed in figure 5c. The impedance spectra are the well-known semicircles. The graph demonstrates a single semicircle representing grain boundary impedance which determines the single relaxation phenomenon.

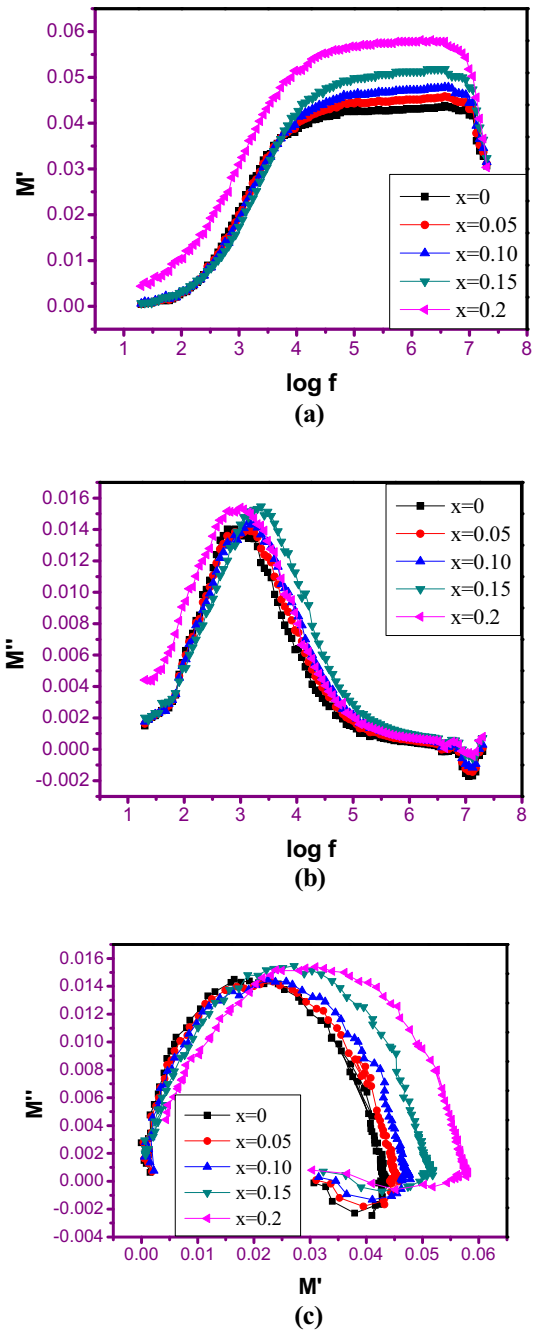

Figure 6. Electric modulus plot of (**a**) real part, (**b**) imaginary part of modulus and (**c**) M' *vs.* M'' plot of $Zr_{1-x}Ca_xTiO_4$ ($x = 0$, 0.05, 0.10, 0.15 and 0.2) samples.

The radii of this semicircle increases with the increase of Ca concentration indicating that at low frequency, resistance of the test material increases.

Moreover, the electric modulus (M^*) plot corresponds to the relaxation of the electric field in the prepared material i.e., when the electric charge displacement remains constant, the real dielectric relaxation process determined by the reciprocal of the permittivity is given by:

$$M^* = \frac{1}{\varepsilon^*} \tag{2}$$

and,

$$M^* = M' + M'' = \frac{\varepsilon'}{\varepsilon'^2 + \varepsilon''^2} + i\frac{\varepsilon''}{\varepsilon'^2 + \varepsilon''^2}, \tag{3}$$

where $M' = \dfrac{\varepsilon'}{(\varepsilon'^2 + \varepsilon''^2)}$ and $M'' = \dfrac{\varepsilon''}{(\varepsilon'^2 + \varepsilon''^2)}$.

Here M' symbolizes the real part and M'' symbolizes the electric modulus of the imaginary part. The frequency dependent spectrum of M' and M'' is designed consulting equation (3) and is shown in figure 6. It can be observed from figure 6a that M' first increases as the concentration of the Ca dopant increases then it shows uniform behaviour which ascertains the relaxation of the electric field of the material. Furthermore, the trend is going to decrease which displays a negligible contribution of the electrode polarization [34].

M'' is plotted with respect to frequency as shown in figure 6b. It is realized from the figure that all the samples show increasing trend and then decrease sharply with frequency. The spectra furthermore show wide and minor kinks that are transferred towards the regions of high frequency side as the Ca content in the ZT sample increases. Figure 6b also presents two regions i.e., low and high frequency regions which explain the range. The low frequency exhibits a time consuming hopping phenomenon among the carriers. The region at high frequency side also represents the charge carriers hopping (actually moveable over a slight distance) which is not time consuming. The total area of the peak represents the mobility of the long to short range. The overall broadening of the peak determines relaxation of the charge carriers with distribution of relaxation of the time constant. Moreover, the peak also indicates the behaviour of the real dielectric relaxation process [35].

The complex electric modulus spectrum for $Zr_{1-x}Ca_xTiO_4$ ($x = 0$, 0.05, 0.10, 0.15 and 0.2) samples is shown in figure 6c. All plot appearances are semicircular in shape. At the lower side of frequency, curves display capacitive outcome for grain boundary and capacitive outcome for grain appears on the higher side of frequency. Common features of figure 6c are summarized by considering the important facts: (1) the effect of the grain and the grain boundary in low and high frequency regions are respectively shown, (2) at low frequency, the semicircle trend increases and the trend decreases at higher side of frequency with increasing Ca content i.e., from 0 to 0.2 and (3) it is seen that with the increase of Ca doping, the intercept in the lower region of frequency on the axis of M' displays that the graph is transferred towards high M' value. The intercept in the higher region of frequency on the axis of M' displays that the graph is transferred to the low M' value, and is indicative of rise in capacitance. Since capacitance and resistance are inversely related, it

furthermore defines the material's behaviour i.e., the negative temperature coefficient of resistance which is usually noticed in temperature-dependent material's dielectric property.

4. Conclusion

$Zr_{1-x}Ca_xTiO_4$ ($x = 0$, 0.05, 0.10, 0.15 and 0.2) ceramics have been synthesized using the sol–gel auto-combustion process. Formation of the impurity free orthorhombic phase for undoped and Ca-doped samples is ascertained through XRD analysis. There is an increase in crystallite size with 0.05 of Ca content and then it displays dissimilarity as the Ca content increases. In accordance with XRD analysis, the FE-SEM and EDS study reveal that the particle size varies from 0.5 to 0.125 μm with increasing Ca content. FTIR study reveals that the organic content does not exist in the prepared samples in the 4000–650 cm^{-1} range. The dielectric study presents the usual dielectric behaviour i.e., it decreases with increasing doping content and frequency, mostly explained by Koop's theory and Maxwell Wagner's polarization model. Conductivity of the material rises with increasing Ca concentration and frequency. Complex impedance analysis of all the prepared samples at low frequency displays a semicircle following ZT and Ca-doped ZT signifying the dominance of grain boundary resistance. Accordingly, this composition at low frequency is capable of storing the charge. As a result, the prepared material is suitable for use in energy storage device applications i.e., capacitors.

References

[1] O'reilly T P, Ruytenberg T and Webb A G 2018 *Magn. Reson. Med.* **79** 1781

[2] Gajovic A, Santic A, Djerdj I, Tomasic N, Mogus M A and Su D S 2009 *J. Alloys Compd.* **479** 525

[3] George A, Solomon S, Thomas J K and John A 2012 *Mater. Res. Bull.* **47** 3141

[4] He X, Meng M, He J, Zou Z, Li X, Li Z *et al* 2010 *Catal. Commun.* **12** 165

[5] Wu C Y, Hsieh C H, Lee C W and Wu Y H 2015 *Appl. Phys. Lett.* **106** 053508

[6] Opra D P, Gnedenkov S V, Sinebryukhov S L, Voit E I, Sokolov A A, Modin E B *et al* 2017 *J. Mater. Sci. Technol.* **33** 527

[7] Tumuluri A, Raju P M S, Raju K J, Seshubai V and Rajasekharan T 2015 *Mater. Lett.* **154** 128

[8] Pang L X, Wang H, Zhou D and Yao X 2009 *Jpn. J. Appl. Phys.* **48** 051403

[9] Wang L, Wang L, Wang Z, Huang B, Zhang Q and Fu Z 2016 *J. Mater. Sci. Mater. Electron.* **27** 3929

[10] Polliotto V, Albanese E, Livraghi S, Indyka P, Sojka Z, Pacchioni G *et al* 2017 *J. Phys. Chem. C* **121** 5487

[11] Fang Z X, Tang B, Long M Z and Zhang S R 2016 *Ceram. Silik.* **60** 122

[12] Wei Z R, Shi C Y, Shen B, Fan M and Wang C 2016 *Materials science forum*, Vol. 852 (Princeton, NJ: Trans Tech Publications) p 272

[13] Ctibor P, Kubatik T, Sedlaek J and Kotlan 2016 *J. Mater. Sci.* **22** 435

[14] Xu C, Yao Z, Lu K, Hao H, Yu Z, Cao M *et al* 2016 *Ceram. Int.* **42** 16109

[15] Dutta H, Nandy A and Pradhan S K 2016 *J. Phys. Chem. Solids* **95** 56

[16] Chang D A, Lin P and Tseng T Y 1995 *J. Appl. Phys.* **77** 4445

[17] Mazur M, Wojcieszak D, Domaradzki J, Kaczmarek D, Poniedziałek A and Domanowski P 2015 *Mater. Res. Bull.* **72** 116

[18] Minagar S, Berndt C C, Gengenbach T and Wen C 2014 *J. Mater. Chem. B* **2** 71

[19] Mattsson A, Lejon C, Bakardjieva S, Stengl V and Osterlund L 2013 *J. Solid State Chem.* **199** 212

[20] Akhtar N, Rafique H M, Atiq S, Aslam S, Razaq A and Saleem M 2018 *Ceram. Int.* **44** 6705

[21] Macan J, Gajovic A, Dekanic D and Ivankovic H 2007 *10th Int. Conf. Exhib. Eur. Ceram. Soc.*, p 866

[22] Kumari R, Sahai A and Goswami N 2015 *Prog. Nat. Sci. Mater. Int.* **25** 300

[23] Keyzer E N, Matthews P D, Liu Z, Bond A D, Grey C P and Wright D S 2017 *Chem. Commun.* **53** 4573

[24] Bianco A, Paci M and Freer R 1998 *J. Eur. Ceram. Soc.* **18** 1235

[25] Koops C G 1951 *Phys. Rev.* **83** 121

[26] Wagner K W 1913 *Ann. Phys.* **40** 817

[27] Ahmad Z, Atiq S, Abbas S K, Ramay S M, Riaz S and Naseem S 2016 *Ceram. Int.* **42** 18271

[28] Abbas S K, Atiq S, Riaz S, Ramay S M and Naseem S 2017 *Mater. Chem. Phys.* **200** 128

[29] Amin M, Rafique H M, Yousaf M, Ramay S M, Saleem M, Abbas S K *et al* 2017 *J. Mater. Sci. Mater. Electron.* **28** 17234

[30] Anantha P S and Hariharan K 2005 *Mater. Sci., Eng. B* **121** 12

[31] Demirezen S, Kaya A, Yerişkin S A, Balbaşı M and Uslu I 2016 *Results Phys.* **6** 180

[32] Altındal Y S, Balbaşı M and Tataroglu A 2016 *J. Appl. Polym. Sci.* **133** 43827

[33] Kakade S G, Ma Y R, Devan R S, Kolekar Y D and Ramana C V 2016 *J. Phys. Chem. C* **120** 5682

[34] Ozogut U C and Cakır A 2017 *J. Alloys Compd.* **705** 126

[35] Guidara S, Feki H and Abid Y 2016 *J. Alloys Compd.* **663** 424